CHIN. PHYS. LETT. Vol. 37, No. 6 (2020) 066401 **Express Letter**

# Pressure-Induced Topological and Structural Phase Transitions in an Antiferromagnetic Topological Insulator *

Cuiying Pei(裴翠颖)[1†], Yunyouyou Xia(夏云悠悠)[1,2,3†], Jiazhen Wu(邬家臻)[4], Yi Zhao(赵毅)[1], Lingling Gao(高玲玲)[1], Tianping Ying(应天平)[4], Bo Gao(高波)[5], Nana Li(李娜娜)[5], Wenge Yang(杨文革)[5], Dongzhou Zhang(张东舟)[6], Huiyang Gou(缑慧阳)[5], Yulin Chen(陈宇林)[1,7,8], Hideo Hosono(细野秀雄)[4], Gang Li(李刚)[1,8**], Yanpeng Qi(齐彦鹏)[1**]

[1]*School of Physical Science and Technology, ShanghaiTech University, Shanghai 201210, China*
[2]*Shanghai Institute of Optics and Fine Mechanics, Chinese Academy of Sciences, Shanghai 201800, China*
[3]*University of Chinese Academy of Sciences, Beijing 100049, China*
[4]*Materials Research Center for Element Strategy, Tokyo Institute of Technology, Yokohama 226-8503, Japan*
[5]*Center for High Pressure Science and Technology Advanced Research (HPSTAR), Shanghai 201203, China*
[6]*Hawai'i Institute of Geophysics and Planetology, School of Ocean and Earth Science and Technology, University of Hawai'i at Manoa, Honolulu, Hawaii 96822, USA*
[7]*Department of Physics, Clarendon Laboratory, University of Oxford, Oxford OX1 3PU, UK*
[8]*ShanghaiTech Laboratory for Topological Physics, ShanghaiTech University, Shanghai 200031, China*

(Received 17 April 2020)

*Recently, natural van der Waals heterostructures of $(MnBi_2Te_4)_m(Bi_2Te_3)_n$ have been theoretically predicted and experimentally shown to host tunable magnetic properties and topologically nontrivial surface states. We systematically investigate both the structural and electronic responses of $MnBi_2Te_4$ and $MnBi_4Te_7$ to external pressure. In addition to the suppression of antiferromagnetic order, $MnBi_2Te_4$ is found to undergo a metal–semiconductor–metal transition upon compression. The resistivity of $MnBi_4Te_7$ changes dramatically under high pressure and a non-monotonic evolution of $\rho(T)$ is observed. The nontrivial topology is proved to persist before the structural phase transition observed in the high-pressure regime. We find that the bulk and surface states respond differently to pressure, which is consistent with the non-monotonic change of the resistivity. Interestingly, a pressure-induced amorphous state is observed in $MnBi_2Te_4$, while two high-pressure phase transitions are revealed in $MnBi_4Te_7$. Our combined theoretical and experimental research establishes $MnBi_2Te_4$ and $MnBi_4Te_7$ as highly tunable magnetic topological insulators, in which phase transitions and new ground states emerge upon compression.*

*PACS:* 64.70.Tg, 03.65.Vf, 07.35.+k DOI: 10.1088/0256-307X/37/6/066401

Magnetic topological insulators (MTIs), possessing both magnetic and topological properties, provide a promising material platform for the realization of exotic topological quantum phenomena, such as the quantum anomalous Hall (QAH) effect, axion insulator states, the proximity effect and Majorana modes.[1–6] Thereinto the QAH effect has been observed experimentally in magnetically doped topological insulator (TI) thin films,[7] while the fabrication of homogeneous thin films has long been limited by deposition techniques, hindering extensive studies of the unique material systems. Hence, intrinsic MTIs with homogeneous magnetic and electronic properties are desired and can provide new opportunities to study novel topological quantum phenomena.

Recently, intrinsic MTIs of $(MnBi_2Te_4)_m(Bi_2Te_3)_n$ has been theoretically predicted and experimentally synthesized to have tunable magnetic properties and topologically nontrivial surface states.[11–23] As shown in Fig. 1, $(MnBi_2Te_4)_m(Bi_2Te_3)_n$ crystallizes in a van der Waals layered structure, sharing a similar crystal structure with $Bi_2Te_3$,[8] a typical TI under ambient conditions. Crystallizing in a rhombohedral structure with space group $R\bar{3}m$, $MnBi_2Te_4(m = 1, n = 0)$ consists of Te-Bi-Te-Mn-Te-Bi-Te septuple layers (SLs) as the building block, each of which can be viewed as a $Bi_2Te_3$ quintuple layer (QL) intercalated by a MnTe bilayer. $MnBi_4Te_7$ $(m = 1, n = 1)$ adopts space group $P\bar{3}m1$ with a hexagonal superlattice crystal structure with alternate stacking of one $MnBi_2Te_4$ SL and one $Bi_2Te_3$ QL. $MnBi_2Te_4$ and $MnBi_4Te_7$ are both identified to be natural van der Waals heterostructures as evidenced by high-angle annular dark field (HAADF)-STEM measurements.[12]

Pressure as a conventional thermodynamic parameter is a clean and useful means to tune the interatomic distance and consequently, can be used to engineer the electronic and, subsequently, the macroscopic physical properties of the system. In addition, it is possible to trigger novel structural and/or electronic

*Supported by the National Key Research and Development Program of China under Grant Nos. 2018YFA0704300 and 2017YFE0131300, the National Natural Science Foundation of China under Grant Nos. U1932217, 11974246, 11874263 and 10225417, and the Natural Science Foundation of Shanghai under Grant No. 19ZR1477300. The authors thank the support from Analytical Instrumentation Center (SPST-AIC10112914), SPST, ShanghaiTech University. This work was partially supported by Collaborative Research Project of Materials and Structures Laboratory, Tokyo Institute of Technology, Japan. Part of this research is supported by COMPRES (NSF Cooperative Agreement EAR-1661511).

†These authors contributed equally to this work.
**Corresponding authors. Email: qiyp@shanghaitech.edu.cn; ligang@shanghaitech.edu.cn

transitions. Indeed, we recently observed pressure-induced topological phase transitions and even superconductivity in topological materials.[24–27] In this work, we study the effect of pressure on the electrical transport properties and crystal structures of $MnBi_2Te_4$ and $MnBi_4Te_7$ in a diamond anvil cell (DAC) apparatus. The antiferromagnetic (AFM) metallic ground state of $MnBi_2Te_4$ and $MnBi_4Te_7$ single crystal is gradually suppressed by pressure, and the conductance as well as the crystal structure change dramatically upon further compression. Through *ab initio* band structure calculations, we find that the application of pressure does not qualitatively change the electronic and topological nature of the two systems until the structural phase transition is observed in the high-pressure regime. Based on synchrotron XRD and Raman spectroscopy measurements, detailed high-pressure crystal structure and phase transitions are discussed.

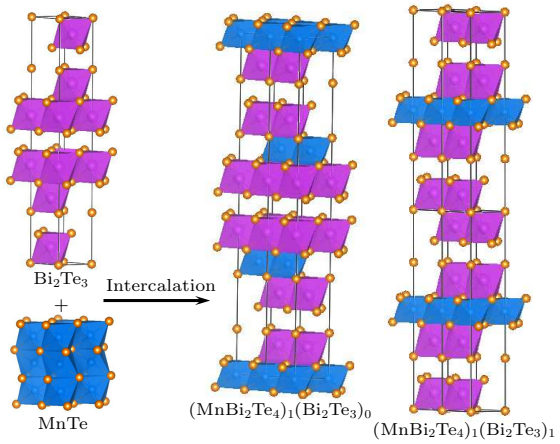


**Fig. 1.** Crystal structure of $Bi_2Te_3$ ($R\bar{3}m$, No. 166),[8] MnTe ($P6_3/mmc$, No. 194),[9] $MnBi_2Te_4$ ($(MnBi_2Te_4)_1(Bi_2Te_3)_0$, $R\bar{3}m$, No. 166)[10] and $MnBi_4Te_7$ ($(MnBi_2Te_4)_1(Bi_2Te_3)_1$, $P\bar{3}m1$, No. 164),[11] respectively. The $MnBi_2Te_4$ unit cell consists of three septuplet monoatomic layers with a stacking sequence of Te(1)-Bi(1)-Te(2)-Mn(1)-Te(2)-Bi(1)-Te(1) along the $c$-axis, and the seven monoatomic layers are centro-symmetrical with respect to Mn. In detail, Mn crystallographic sites are of octahedral coordination and are surrounded by six Te(2) atoms at the same distance as under ambient conditions. Bi is at the center of a distorted octahedron and is surrounded by three Te(2) atoms and three Te(1) atoms as the nearest neighbors. Triple slabs of $MnTe_6$ and $BiTe_6$ are octahedral edge-linked with each other, and similarly for the SL of $MnBi_4Te_7$. Alternation of QL (Te(2)-Bi(1)-Te(1)-Bi(1)-Te(2)) and SL (Te(3)-Bi(2)-Te(4)-Mn(1)-Te(4)-Bi(2)-Te(3)) blocks stack along the $c$-axis and $MnBi_4Te_7$ is in the trigonal space group $P\bar{3}m1$.

The $MnBi_2Te_4$ and $MnBi_4Te_7$ single crystals in this work were grown using a flux-assisted method.[12] High-pressure resistivity measurements were performed in a nonmagnetic DAC. A cubic BN/epoxy mixture layer was inserted between BeCu gaskets and electrical leads. Four Pt foils were arranged in a van der Pauw four-probe configuration to contact the sample in the chamber for resistivity measurements. NaCl was used as the pressure transmitting medium (PTM) and pressure was determined by the ruby luminescence method.[28]

An *in situ* high-pressure Raman spectroscopy investigation of $MnBi_2Te_4$ and $MnBi_4Te_7$ was performed using a Raman spectrometer (Renishaw inVia, UK) with a laser excitation wavelength of 532 nm and low-wavenumber filter. A symmetric DAC with anvil culet sizes of 400 μm was used, with silicon oil as the PTM. The *in situ* high-pressure XRD measurements were performed at beamline 13-BM-C of the Advanced Photon Source (APS) (x-ray wavelength $\lambda = 0.4340$ Å) and beamline BL15U of Shanghai Synchrotron Radiation Facility (x-ray wavelength $\lambda = 0.6199$ Å). Symmetric DACs with anvil culet sizes of 400 μm and 300 μm and T301 gaskets were used. Neon was used as the PTM and pressure was determined by the ruby luminescence method.[28] The two-dimensional diffraction images were integrated into angle-resolved diffraction intensity profiles using the software DIOPTAS.[29] Rietveld refinements on crystal structures under high pressure were performed using the General Structure Analysis System (GSAS) and the graphical user interface EXPGUI.[30]

The *ab initio* calculations were performed within the framework of density functional theory (DFT) as implemented in the Vienna *ab initio* simulation package (VASP),[31] with the exchange-correlation functional considered in the generalized gradient approximation potential.[32] A k-mesh of $9 \times 9 \times 1$ for $MnBi_2Te_4$ and $9 \times 9 \times 3$ for $MnBi_4Te_7$ was applied. The experimental lattice constants were adopted under different pressures with atomic positions optimized for a total energy tolerance of $10^{-5}$ eV. To account for the correlation effect of the transition metal element Mn in both $MnBi_2Te_4$ and $MnBi_4Te_7$, the GGA+$U$ functional with $U = 3$ eV for the $d$-orbitals of Mn is adopted. The spin–orbital coupling was considered self-consistently in this work. The topological surface states were calculated by applying the iterative Green's function approach[33] as implemented in WannierTools[34] based on the maximally localized Wannier functions[35] as obtained through the VASP2WANNIER90[36] interfaces in a non-self-consistent calculation.

As a typical layered material, the electrical transport and magnetic properties of $MnBi_2Te_4$ and $MnBi_4Te_7$ are expected to be sensitive to the competition between interlayer and intralayer interactions, which can be effectively tuned by applying external pressure. We performed resistivity measurements on several single crystals at various pressures. Figures 2(a), 2(b), and 2(c) show the typical $\rho(T)$ curves of $MnBi_2Te_4$ for pressures up to 34.0 GPa. As shown in Fig. 2(a), the resistivity–temperature slope $d\rho/dT$ of $MnBi_2Te_4$ clearly shows a positive value, indicating metal-like conduction in the low-pressure range. With an increase of pressure, $\rho(T)$ curves show an upturn behavior at low temperatures. Upon further compression, a metal–semiconductor transition is observed and $\rho(T)$ displays a semiconductor-like behav-

ior for $P > 12$ GPa. Interestingly, the resistivity ultimately undergoes a metallization at a pressure above 16.3 GPa and does not change significantly in response to further increases in the pressure. No superconductivity was observed down to 1.8 K in this pressure range.

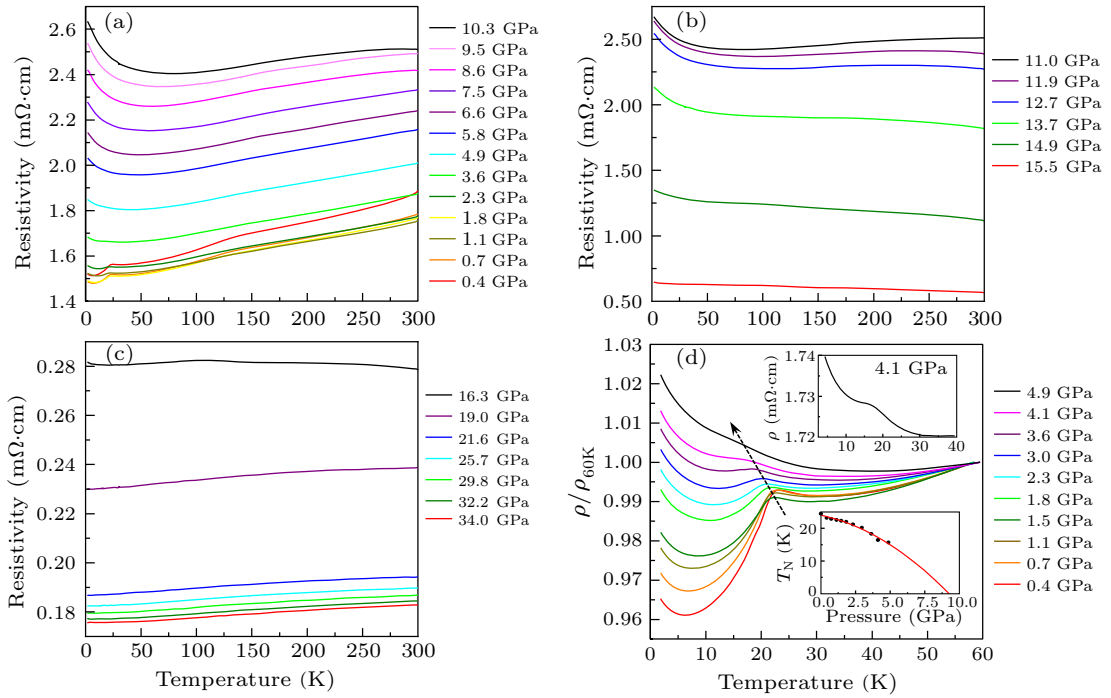


**Fig. 2.** Electrical resistivity of $MnBi_2Te_4$ as a function of temperature for pressures up to 10.3 GPa (a), 15.5 GPa (b) and 34.0 GPa (c); (d) detail of the normalized resistivity of $MnBi_2Te_4$ as a function of temperature at various pressures to monitor the shift of the AFM transition kink. The inset shows the enlarged resistivity–temperature curve at 4.1 GPa and fitting of the AFM transition temperature as a function of pressure.

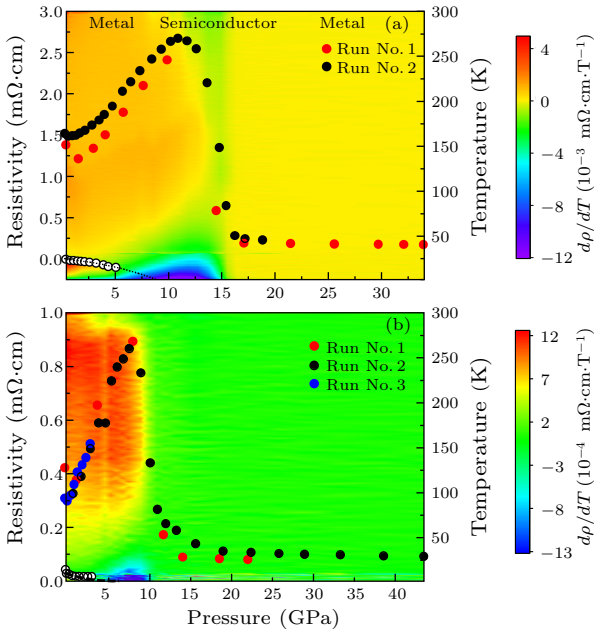


**Fig. 3.** Electronic phase diagrams of $MnBi_2Te_4$ (a) and $MnBi_4Te_7$ (b). The black, blue and red solid circles represent different runs of electrical resistivity measurements at 1.8 K. The black open circles indicate AFM transition temperatures due to the transport measurements.

It should be noted that $\rho(T)$ of $MnBi_2Te_4$ displays a kink at the AFM transition $T_N = 24.5$ K at 0.4 GPa (Fig. 2(d)), which is consistent with the magnetic measurements shown in Fig. S1 (see the Supplemental Material) and those in other reports.[20] The rapid drop of resistivity below $T_N$ is attributed to the reduction of spin scattering after the formation of long-range AFM order.[37] As indicated by the arrow in Fig. 2(d), $T_N$ determined from the resistivity kink shifts to lower temperatures with increasing pressure. Over 4.9 GPa, the upturn resistivity trend at lower temperature becomes much stronger and the kink merges into the $\rho(T)$ curve. The fitting results demonstrate that $T_N$ approaches zero at approximately 9.3 GPa. Since the interlayer distance deceases under high pressure, it is speculated that the pressure-induced enhancement of antiferromagnetic/ferromagnetic competition and the partial delocalization of Mn-3$d$ electrons not only destroys long-range AFM order, but also promotes charge-carrier localization through enhanced spin fluctuations and/or the formation of a hybridization gap at high pressure.

The high-pressure experiments have been repeated on different samples with good reproducibility of the observed transition temperatures. Based on the above resistivity measurements, we summarize a $T$–$P$ phase diagram for $MnBi_2Te_4$ single crystals in Fig. 3(a). The resistivity of $MnBi_2Te_4$ shows non-monotonic evolution with increasing pressure. Over the entire temperature range, the resistivity is first suppressed with applied pressure and reaches a minimum value at about

2 GPa. As the pressure further increases, the resistivity increases with a maximum occurring at 11.0 GPa and the AFM order shifted to a lower temperature. Accompanying the suppression of the AFM transition, the electrical transport properties also change qualitatively from metal-like $d\rho/dT > 0$ to semimetal- or semiconducting-like behavior $d\rho/dT < 0$. For $P > 12$ GPa, the resistivity abruptly decreases and a transition from semiconducting to metallic behavior takes place at further increased pressure. Similarly, pressure-induced non-monotonic evolution was also observed in $MnBi_4Te_7$, as shown in Fig. 3(b). Although resistivity changes significantly under high pressure, $\rho(T)$ exhibits a metallic behavior over the whole temperature range (Fig. S2). No transition from metallic to semiconducting behavior was observed within the studied pressure range. The AFM order of $MnBi_4Te_7$ shifted to a lower temperature with increasing pressure, which is similar to that of $MnBi_2Te_4$ (Fig. S3).

The angular dispersive XRD patterns of $MnBi_2Te_4$ at various pressures are shown in Fig. 4(a). Under ambient conditions and in the low-pressure range ($P \leq 14.6$ GPa), all the diffraction peaks of $MnBi_2Te_4$ could be indexed to the rhombohedral $R\bar{3}m$ (No. 166) structure by Rietveld refinement (Fig. 4(b)). High-pressure XRD experiments in pressure steps of 1–2 GPa were performed on $MnBi_2Te_4$ via a DAC. At pressures exceeding 14.6 GPa, structural disorder becomes apparent. Above 17.4 GPa, diffraction peaks from crystalline phase disappear, and a new broad peak appears at approximately 2.65 Å in $d$-spacing. This indicates that the sample has completely transformed into an amorphous state.

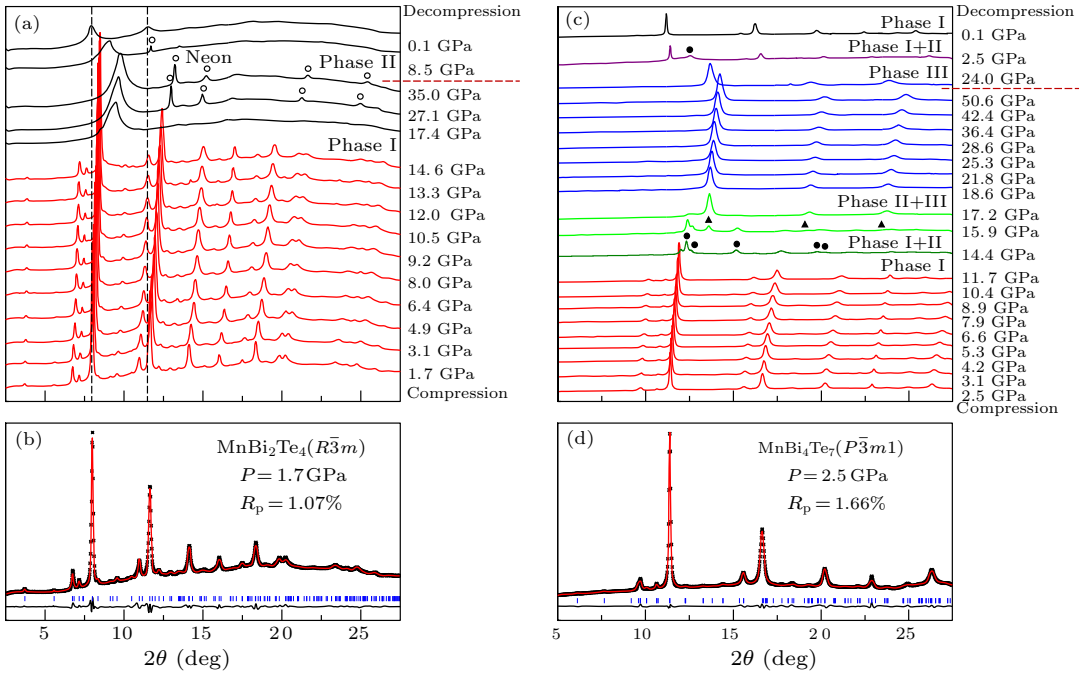


**Fig. 4.** XRD patterns collected at various pressures for $MnBi_2Te_4$ with an x-ray wavelength of $\lambda = 0.4340$ Å (a) and $MnBi_4Te_7$ with an x-ray wavelength of $\lambda = 0.6199$ Å (c); the black open circles are from PTM neon; typical Rietveld refinement of phase I of $MnBi_2Te_4$ (b) and $MnBi_4Te_7$ (d), respectively. The experimental and simulated data are indicated by black stars and red lines, respectively. The solid lines shown at the bottom of the figures are the residual intensities. The vertical bars indicate peak positions.

In contrast, a different structure evolution for $MnBi_4Te_7$ is observed under high pressure (Fig. 4(c)). In the low-pressure range, phase I of $MnBi_4Te_7$ crystallizes in a trigonal space group $P\bar{3}m1$ (No. 164), as shown in Fig. 4(d). At 14.4 GPa, a high-pressure phase, phase Ⅱ, was observed. This phase is only stable in a narrow pressure range and coexists with the phase I or the phase Ⅲ upon compression. Above 18.6 GPa, only phase Ⅲ exists and no further transitions are observed up to 50.6 GPa. Upon decompression, phase Ⅲ persists to 24.0 GPa. When the pressure is decreased to 2.5 GPa, phase Ⅱ and phase I recover and coexist. After a full pressure release, $MnBi_4Te_7$ recovers the ambient-pressure structure.

To verify our speculation on the crystallographic structural phase transition sequence under high pressure, Raman scattering spectroscopy was employed to characterize the pressure-induced phase transition (Fig. 5(a)). According to group theory analysis and the results in the literature,[38] there are four Raman-active modes ($2E_g + 2A_{1g}$) for $MnBi_2Te_4$. The $E_g$ and $A_{1g}$ modes are related to the in-plane $A$(VI)–$B$(V) and out-of-plane lattice vibrations, respectively (Fig. 5(b)). At 0.3 GPa, four peaks are assigned as follows: 47.4 $cm^{-1}$($E_g$), 67.4 $cm^{-1}$($A_{1g}$), 104.2 $cm^{-1}$($E_g$), and 139.8 $cm^{-1}$($A_{1g}$).[38] As the pressure increases, all four modes exhibit blue shift due to the increase in the strength of the Bi–Te covalent interaction (Fig. 5(c)). Upon further compression

exceeding a pressure of 17.8 GPa, all the peaks disappear. The pressure-induced amorphization occurs at 17.8 GPa, which coincides with the XRD result at 17.4 GPa. In addition, a reversible phase transition associated with a compressed lattice (where the lattice constants are decreased) is verified by the Raman spectrum of the sample after recovery to 1 atm. The Raman spectra of $MnBi_4Te_7$ were also measured using a DAC and a similar phenomenon was observed under high pressure (Fig. S4). It should be noted that no new Raman modes were observed under higher pressure, although a structural phase transition is observed by synchrotron XRD measurements. One can expect that pressure-induced metallization or vibration modes become weaker under high pressure, which may account for the absence of Raman modes.

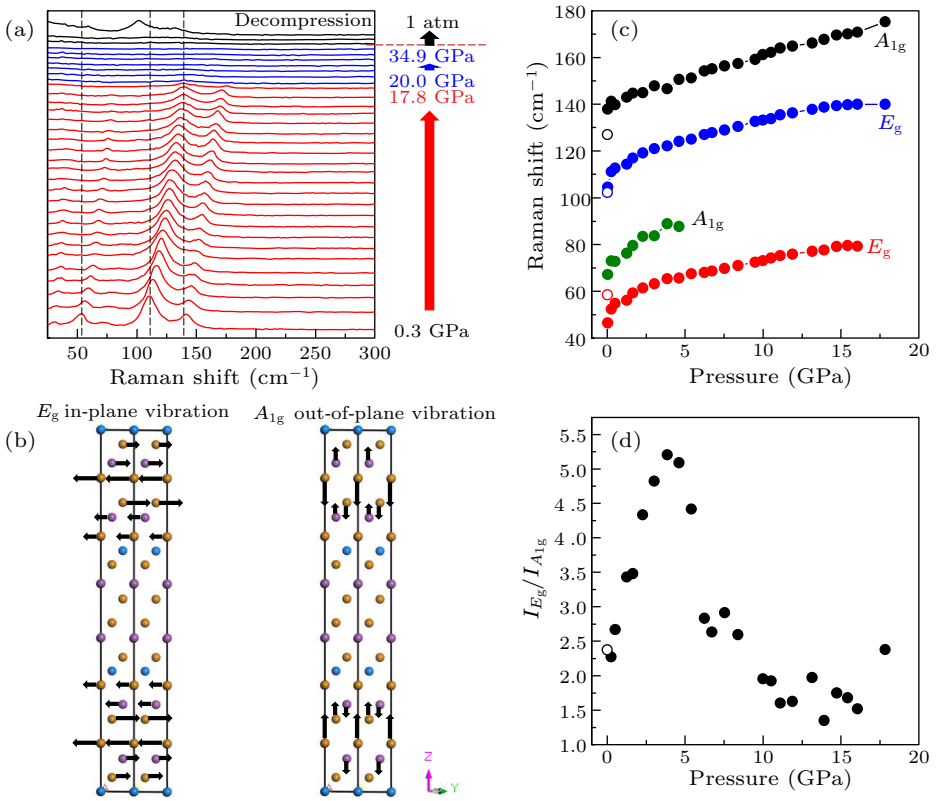


**Fig. 5.** (a) Raman spectra at various pressures for $MnBi_2Te_4$; (b) phonon mode symmetry and direction of vibration for $MnBi_2Te_4$; (c) Raman mode frequencies for $MnBi_2Te_4$ in compression (solid circle) and decompression (open circle); (d) pressure dependence of $I_{E_g}/I_{A_{1g}}$ intensity ratio for $MnBi_2Te_4$. For accurate peak intensity comparison, the strong $E_g$ and $A_{1g}$ modes with respective Raman shifts of 104.2 cm$^{-1}$ and 139.8 cm$^{-1}$ at 1 atm are chosen. Peak intensity and peak position are obtained by Gaussian and Lorentzian mixed line shape fitting. Open circles represent data recovered for 1 atm.

To understand the non-monotonic change of the measured resistivity under different pressures, we performed detailed *ab initio* calculations and examined both the bulk and surface electronic structures of $MnBi_2Te_4$ (Figs. 6 and S5). Electron transportation is mainly determined by the states around the Fermi level which can be effectively tuned by external pressure. Concerning a topological system, these states contain both the bulk and the topological surface/edge contributions. It is widely known that the topology of a topological system is fully determined by the symmetry and the associated Berry curvature of the bulk bands. As long as they are qualitatively unchanged, the topology persists (Fig. S5). However, external perturbations, such as the pressure, can modify the dispersions of both the bulk and surface bands, resulting in different transport responses. In Fig. 6(a) the electronic structures of $MnBi_2Te_4$ are displayed for different pressures. $MnBi_2Te_4$ is a semiconductor with a gap of 243.4 meV at atmospheric pressure. Once external pressure is applied, the conduction band bottom changes from $Z$ to $\Gamma$ and the gap size gradually decreases with increasing pressure. At the highest pressure applied which maintains the crystal symmetry of $MnBi_2Te_4$, a global gap remains but it is significantly reduced to 16.3 meV.

Due to the topological nature of this system, the total conductance/resistance experimentally measured is subjected to contributions from both the bulk and surface electrons. We, thus, further determined the surface electronic structure of the experimentally cleaved (001) surface (Fig. 6(b)). In sharp contrast to the bulk electronic structure, an overall reentrant behavior of the gapped surface states is observed upon

the increase of pressure. Below 4.9 GPa, the magnetic surface states move from below to above the Fermi level, leading to a metal–semiconductor transition solely caused by the surface electrons. The surface states, with a clear separation from the bulk bands at pressures below 4.9 GPa, completely merge into the bulk bands at pressures above 10.5 GPa. Above this pressure, the contribution to the resistivity is mainly determined by the bulk gap and electrons. Thus, the decrease in the bulk gap results in a decrease of the resistivity as shown in Fig. 3(a) above 10.5 GPa. However, below 10.5 GPa, the bulk and surface electrons behave differently, i.e., the surface electrons are gradually localized, and the bulk electrons become more mobile with increasing pressure. Thus, the competition between the two types of electrons results in the decrease–increase behavior of the resistivity observed in Fig. 3(a). More precisely, we suspect that the decrease in the resistivity below 3.1 GPa is mainly induced by the delocalization of the bulk electrons as the surface electrons remain metallic; while the increase in the resistivity is mainly a consequence of the localization of the surface electrons, as the surface states are no longer metallic and have not yet merged into the bulk states.

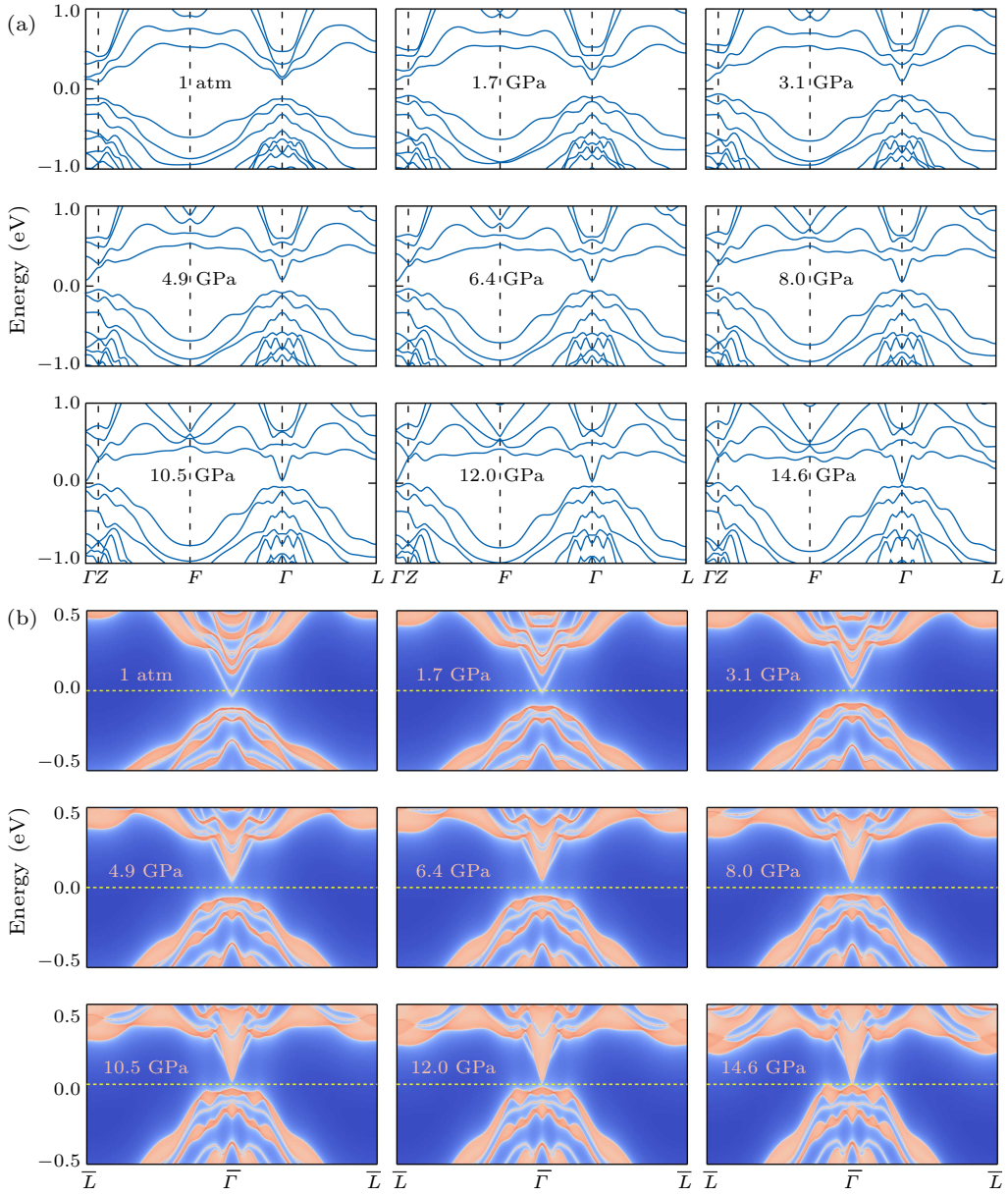


**Fig. 6.** Bulk and surface electronic structures of $MnBi_2Te_4$ at different pressures. (a) The bulk electronic structure remains gapped under all applied pressures with roughly monotonic decrease of gap size. (b) The topological surface states on (001) display a reentrant behavior upon the increase of pressure.

A similar analysis can be applied to $MnBi_4Te_7$ (Figs. S5 and S6). We note that the bulk gap shown in Fig. S6(a) decreases under increasing pressure with the minimum gap decreasing from 196.7 meV to 174.8 meV at $\Gamma$, which only renders more substantial contribution to its conductance at higher pressures. At low pressure, the contribution from the surface states becomes dominant. As $MnBi_4Te_7$ can be naturally cleaved at $MnBi_2Te_4$ and $Bi_2Te_3$ layers, the total surface conductance includes components from both terminations. The topological surface states with $MnBi_2Te_4$ termination intersect the Fermi level under all examined pressures (Fig. S6(b)), presenting a metallic background in the measured pressure range. Meanwhile, the surface electrons terminated at $Bi_2Te_3$ become more localized with increasing pressure. The surface band crosses the Fermi level at 2.5 GPa, and gradually moves to higher binding energies with further increase of pressure. The competition between the two types of electrons again results in the decrease–increase behavior of resistivity observed in Fig. 3(b). Below 2.5 GPa, the delocalization of the bulk electrons is attributed to the decrease of resistivity, while the subsequent increase of the resistivity above 2.5 GPa mainly stems from the localization of the surface electrons. At approximately 10.4 GPa, the surface bands merge into the bulk states, after which the resistivity is mainly determined by the bulk electrons, and thus shows a sharp decline as observed in the transport measurements.

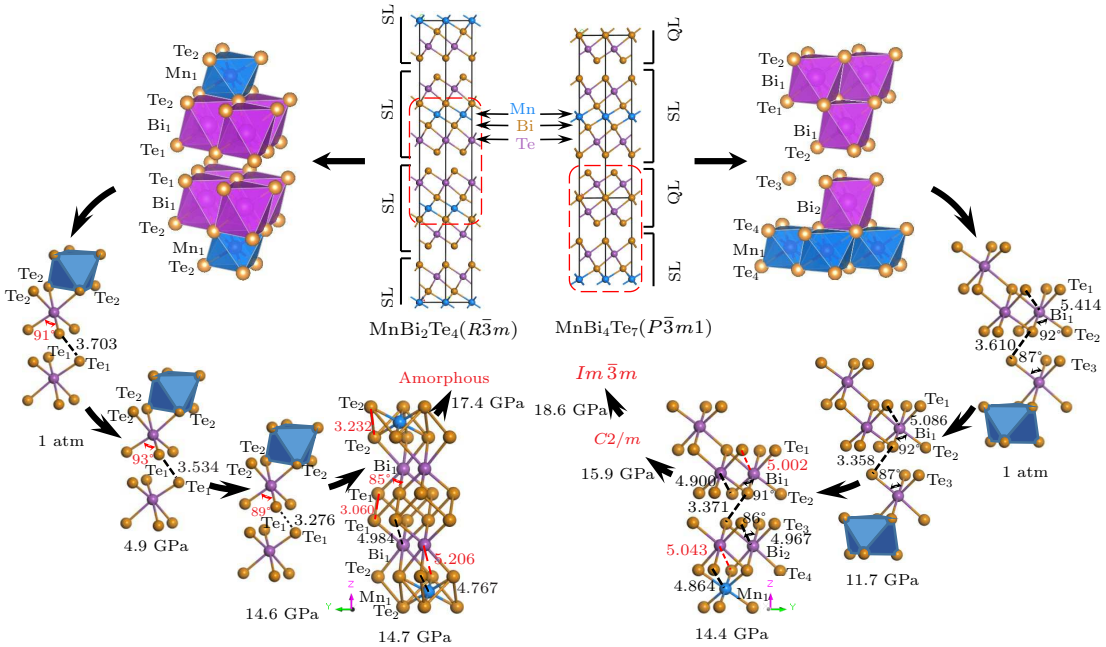


**Fig. 7.** Schematic representation of the evolution of $MnBi_2Te_4$ and $MnBi_4Te_7$ structures under high pressure.

Next, we discuss the high-pressure phase transition. To gain an insight into the structural evolution, pressure-induced bond length and angle variations in $MnTe_6$ and $BiTe_6$ octahedra are derived from the Rietveld refinements (Fig. S7). The Mn–Te bond length decreases with an increase of pressure and the bond angle of Te(2)–Mn(1)–Te(2) changes only slightly (Figs. S7(a) and S7(b)). Below 3.1 GPa, the pressure coefficients of Bi(1)–Te(1) and Bi(1)–Te(2) bond lengths show the same sign. Also, both the Te(1)–Bi(1)–Te(1) bond angle and the distance between the two Te(1)'s of the near neighbor septuple blocks decrease with increasing pressure (Figs. S7c and S7d). However, Bi(1)–Te(2) and Bi(1)–Te(1) bond lengths show opposite responses to pressure near 4 GPa, and Te(1)–Bi(1)–Te(1) bond angle also behaves differently from Te(1)–Bi(1)–Te(2) and Te(2)–Bi(1)–Te(2) bond angles (Figs. S7(c) and S7(d)). These results indicate that the distorted octahedral $BiTe_6$ deforms more significantly above 3.1 GPa and bends towards Mn atoms (Fig. S7(e)). This releases stress along the $c$-axis and weakens the interaction between the nearest neighbor SL. Upon further compression, interlayer interaction enhancement dominates and ultimately the interlayer Te(1)–Te(1) bond is formed. The pressure dependence of the $c/a$ ratio for the $R\bar{3}m$ phase of $MnBi_2Te_4$ (plotted in Fig. S8(a)) shows a minimum at approximately 3.1 GPa. This is consistent with the Raman spectroscopy observations. The in-plane Bi–Te vibration was enhanced significantly with pressure. With further compression, the ratio of out-of-plane Bi–Te vibrations is enhanced when the pressure exceeds 3.8 GPa as shown in the evolution of the intensity ratio ($I_{E_g}/I_{A_{1g}}$) in Fig. 5(d). A similar phenomenon was observed in the $MnBi_4Te_7$ phase (Fig. S4(d)). It is clear that the structural change induced by external pressure will significantly modify the corresponding electronic structure. The reduced interlayer distance

will enhance the three-dimensional dispersion of the system. As a result, the electronic states around the Fermi level will be considerably modified, which, ultimately, influences the macroscopic resistivity. Thus, such layered MTIs with large inter-layer distances are ideal for pressure engineered materials.

In compression, there is a quite distinct compression behavior between $MnBi_2Te_4$ and $MnBi_4Te_7$. Figure 7 shows the pressure-induced structural evolution of $MnBi_2Te_4$ and $MnBi_4Te_7$, respectively. The former transforms to an amorphous phase at approximately 17.4 GPa, while the latter transforms from a rhombohedral to a mixed high-pressure phase at 14.4 GPa, and finally phase Ⅲ obtained at 18.6–50.6 GPa. For phase Ⅱ of $MnBi_4Te_7$, Le Bail refinement yielded a monoclinic structure with $a = 14.4192(3)$ Å, $b = 3.9415(9)$ Å, $c = 17.1202(7)$ Å, and $\beta = 148.62(7)°$. The XRD pattern of phase Ⅲ is simple and can be indexed to an $Im\bar{3}m$ (No. 229) structure with $a = 3.6796(0)$ Å (Fig. S9, Table S1). The different compression behavior is related to the distortion of $MnTe_6$ and $BiTe_6$, which is induced by competition under high pressure. In $MnBi_2Te_4$, the Te(2)–Te(2) bond forms besides Te(1)–Te(1) linked in the low-pressure range accompanied by $MnTe_6$ octahedron flattening. In contrast, the distances of Bi(1)–Te(1) (5.002 Å) and Bi(1)–Te(2) (4.900 Å) are shorter than Bi(2)–Te(4) (5.043 Å) in $MnBi_4Te_7$ and Bi(1)–Te(2) (5.206 Å) in $MnBi_2Te_4$. As a result, the pressure-induced distorted $Bi(1)Te_6$ octahedron in the $Bi_2Te_3$ quintuple block tends to form a heptahedrally coordinated $BiTe_7$ unit and further $Bi(Te)_n$ ($n > 7$). At 18.6 GPa, the Te–Te and Bi–Te distances in $MnBi_4Te_7$ are close to each other because of the flatter $MnTe_6$ octahedron as well as the improved interaction between QL and SL (Fig. S10). An alternating Bi, Te structure with Mn intercalation exists during the formation of an isotropic phase along the layers and perpendicular to the layers. The structural evolution of $MnBi_4Te_7$ under high pressure resembles the situation in the case of $Bi_2Te_3$.[8,39,40] Recent sister compounds $MnBi_6Te_{10}$ ($m = 1$, $n = 2$) and $MnBi_8Te_{13}$ ($m = 1$, $n = 3$) have been grown successfully.[41–44] It will be interesting to characterize the structural evolution of this series $(MnBi_2Te_4)_m(Bi_2Te_3)_n$ of compounds and summarize pressure-induced phase transition in these layered compounds.

In conclusion, we have performed a comprehensive high-pressure study on the electrical transport properties and crystal structures of the MTIs $MnBi_2Te_4$ and $MnBi_4Te_7$ in DACs. The AFM metallic ground state of $MnBi_2Te_4$ and $MnBi_4Te_7$ single crystals are gradually suppressed by pressure. The pressure-dependent resistivity over a wide temperature range passes through a minimum at around 3 GPa. Upon further increasing the pressure, resistivity starts to increase rapidly, reaching a maximum at a pressure above 10 GPa. Through *ab initio* calculations, we find that the application of pressure does not destroy the nontrivial topology of the system before structural phase transition. However, the bulk and surface states respond differently to external pressure, resulting in competing contributions to the macroscopic resistivity. Based on synchrotron XRD and Raman spectroscopy measurements, we find that $MnBi_2Te_4$ transforms to an amorphous phase at around 17.4 GPa, while $MnBi_4Te_7$ transforms to two new high-pressure phases. Application of pressure effectively tuned the electronic properties and crystal structure of $MnBi_2Te_4$ and $MnBi_4Te_7$. Considering both intriguing magnetism and topology in this layered material, our results call for further experimental and theoretical studies on $(MnBi_2Te_4)_m(Bi_2Te_3)_n$ and related materials for a better understanding of the interplay between magnetic and topological nature, and its potential application in realizing topological superconductivity.

We thank Dr. Zhenhai Yu for valuable discussions. We thank the staffs from BL15U1 at Shanghai Synchrotron Radiation Facility for assistance during data collection. Portions of this work were performed at GeoSoilEnviroCARS (The University of Chicago, Sector 13), Advanced Photon Source (APS), Argonne National Laboratory. GeoSoilEnviroCARS is supported by the National Science Foundation-Earth Sciences (EAR-1634415) and Department of Energy-GeoSciences (DE-FG02-94ER14466). This research used resources of the Advanced Photon Source, a U.S. Department of Energy (DOE) Office of Science User Facility operated for the DOE Office of Science by Argonne National Laboratory under Contract Nos. DE-AC02-06CH11357.

## References

[1] Mong R S K, Essin A M and Moore J E 2010 *Phys. Rev. B* **81** 245209
[2] Tokura Y, Yasuda K and Tsukazaki A 2019 *Nat. Rev. Phys.* **1** 126
[3] He Q L, Kou X, Grutter A J, Yin G, Pan L, Che X, Liu Y, Nie T, Zhang B, Disseler S M, Kirby B J, Ratcliff I I W, Shao Q, Murata K, Zhu X, Yu G, Fan Y, Montazeri M, Han X, Borchers J A and Wang K L 2017 *Nat. Mater.* **16** 94
[4] Wray L A, Xu S Y, Xia Y, Hsieh D, Fedorov A V, Hor Y S, Cava R J, Bansil A, Lin H and Hasan M Z 2011 *Nat. Phys.* **7** 32
[5] Šmejkal L, Mokrousov Y, Yan B and MacDonald A H 2018 *Nat. Phys.* **14** 242
[6] Mogi M, Kawamura M, Yoshimi R, Tsukazaki A, Kozuka Y, Shirakawa N, Takahashi K S, Kawasaki M and Tokura Y 2017 *Nat. Mater.* **16** 516
[7] Chang C Z, Zhang J, Feng X, Shen J, Zhang Z, Guo M, Li K, Ou Y, Wei P, Wang L L, Ji Z Q, Feng Y, Ji S, Chen X, Jia J, Dai X, Fang Z, Zhang S C, He K, Wang Y, Lu L, Ma X C and Xue Q K 2013 *Science* **340** 167
[8] Zhu L, Wang H, Wang Y, Lv J, Ma Y, Cui Q, Ma Y and Zou G 2011 *Phys. Rev. Lett.* **106** 145501
[9] Johnston W D and Sestrich D E 1961 *J. Inorg. Nucl. Chem.* **19** 229
[10] Lee D S, Kim T H, Park C H, Chung C Y, Lim Y S, Seo W S and Park H H 2013 *CrystEngComm* **15** 5532
[11] Aliev Z S, Amiraslanov I R, Nasonova D I, Shevelkov A V, Abdullayev N A, Jahangirli Z A, Orujlu E N, Otrokov M M, Mamedov N T, Babanly M B and Chulkov E V 2019 *J. Alloys Compd.* **789** 443

[12] Wu J, Liu F, Sasase M, Ienaga K, Obata Y, Yukawa R, Horiba K, Kumigashira H, Okuma S, Inoshita T and Hosono H 2019 *Sci. Adv.* **5** eaax9989

[13] Gong Y, Guo J, Li J, Zhu K, Liao M, Liu X, Zhang Q, Gu L, Tang L, Feng X, Zhang D, Li W, Song C, Wang L, Yu P, Chen X, Wang Y, Yao H, Duan W, Xu Y, Zhang S C, Ma X, Xue Q K and He K 2019 *Chin. Phys. Lett.* **36** 076801

[14] Zhang D, Shi M, Zhu T, Xing D, Zhang H and Wang J 2019 *Phys. Rev. Lett.* **122** 206401

[15] Li J, Li Y, Du S, Wang Z, Gu B L, Zhang S C, He K, Duan W and Xu Y 2019 *Sci. Adv.* **5** eaaw5685

[16] Hu C, Gordon K N, Liu P, Liu J, Zhou X, Hao P, Narayan D, Emmanouilidou E, Sun H, Liu Y, Brawer H, Ramirez A P, Ding L, Cao H, Liu Q, Dessau D and Ni N 2020 *Nat. Commun.* **11** 97

[17] Chen Y, Xu L, Li J, Li Y, Wang H, Zhang C, Li H, Wu Y, Liang A, Chen C, Jung S W, Cacho C, Mao Y, Liu S, Wang M, Guo Y, Xu Y, Liu Z, Yang L and Chen Y 2019 *Phys. Rev. X* **9** 041040

[18] Hao Y J, Liu P, Feng Y, Ma X M, Schwier E F, Arita M, Kumar S, Hu C, Lu R E, Zeng M, Wang Y, Hao Z, Sun H Y, Zhang K, Mei J, Ni N, Wu L, Shimada K, Chen C, Liu Q and Liu C 2019 *Phys. Rev. X* **9** 041038

[19] Li H, Gao S, Duan S, Xu Y, Zhu K, Tian S, Gao J, Fan W, Rao Z, Huang J, Li J, Yan D, Liu Z, Liu W, Huang Y, Li Y, Liu Y, Zhang G, Zhang P, Kondo T, Shin S, Lei H, Shi Y, Zhang W, Weng H, Qian T and Ding H 2019 *Phys. Rev. X* **9** 041039

[20] Otrokov M M, Klimovskikh I I, Bentmann H, Estyunin D, Zeugner A, Aliev Z S, Gass S, Wolter A U B, Koroleva A V, Shikin A M, Blanco-Rey M, Hoffmann M, Rusinov I P, Vyazovskaya A Y, Eremeev S V, Koroteev Y M, Kuznetsov V M, Freyse F, Sanchez-Barriga J, Amiraslanov I R, Babanly M B, Mamedov N T, Abdullayev N A, Zverev V N, Alfonsov A, Kataev V, Buchner B, Schwier E F, Kumar S, Kimura A, Petaccia L, Di Santo G, Vidal R C, Schatz S, Kissner K, Unzelmann M, Min C H, Moser S, Peixoto T R F, Reinert F, Ernst A, Echenique P M, Isaeva A and Chulkov E V 2019 *Nature* **576** 416

[21] Deng Y, Yu Y, Shi M, Xu Z, Wang J, Chen X and Zhang Y 2020 *Science* **367** 895

[22] Zhang S, Wang R, Wang X, Wei B, Chen B, Wang H, Shi G, Wang F, Jia B, Ouyang Y, Xie F, Fei F, Zhang M, Wang X, Wu D, Wan X, Song F, Zhang H and Wang B 2020 *Nano Lett.* **20** 709

[23] Liu C, Wang Y, Li H, Wu Y, Li Y, Li J, He K, Xu Y, Zhang J and Wang Y 2020 *Nat. Mater.* **19** 522

[24] Qi Y, Naumov P G, Ali M N, Rajamathi C R, Schnelle W, Barkalov O, Hanfland M, Wu S C, Shekhar C, Sun Y, Sü V, Schmidt M, Schwarz U, Pippel E, Werner P, Hillebrand R, Forster T, Kampert E, Parkin S, Cava R J, Felser C, Yan B and Medvedev S A 2016 *Nat. Commun.* **7** 11038

[25] Qi Y, Shi W, Naumov P G, Kumar N, Schnelle W, Barkalov O, Shekhar C, Borrmann H, Felser C, Yan B and Medvedev S A 2016 *Phys. Rev. B* **94** 054517

[26] Qi Y, Shi W, Naumov P G, Kumar N, Sankar R, Schnelle W, Shekhar C, Chou F C, Felser C, Yan B and Medvedev S A 2017 *Adv. Mater.* **29** 1605965

[27] Qi Y, Shi W, Werner P, Naumov P G, Schnelle W, Wang L, Rana K G, Parkin S, Medvedev S A, Yan B and Felser C 2018 *npj Quantum Mater.* **3** 4

[28] Mao H K, Xu J and Bell P M 1986 *J. Geophys. Res.* **91** 4673

[29] Prescher C and Prakapenka V B 2015 *High Press. Res.* **35** 223

[30] Larson A C and Dreele R B V 2004 *Los Alamos Natl. Laboratory Report* LAUR pp 86–748

[31] Kresse G and Furthmüller J 1996 *Phys. Rev. B* **54** 11169

[32] Perdew J P, Burke K and Ernzerhof M 1996 *Phys. Rev. Lett.* **77** 3865

[33] Sancho M P L, Sancho J M L and Rubio J 1985 *J. Phys. F* **15** 851

[34] Wu Q, Zhang S, Song H F, Troyer M and Soluyanov A A 2018 *Comput. Phys. Commun.* **224** 405

[35] Marzari N and Vanderbilt D 1997 *Phys. Rev. B* **56** 12847

[36] Mostofi A A, Yates J R, Lee Y S, Souza I, Vanderbilt D and Marzari N 2008 *Comput. Phys. Commun.* **178** 685

[37] Chen K, Wang B, Yan J Q, Parker D S, Zhou J S, Uwatoko Y and Cheng J G 2019 *Phys. Rev. Mater.* **3** 094201

[38] Mal P, Bera G, Turpu G R, Srivastava S K, Gangan A, Chakraborty B, Das B and Das P 2019 *Phys. Chem. Chem. Phys.* **21** 15030

[39] Einaga M, Ohmura A, Nakayama A, Ishikawa F, Yamada Y and Nakano S 2011 *Phys. Rev. B* **83** 092102

[40] Guo Z, Zhu H, Dong J, Jia Q, Gong Y, Wang Y, Li H, An P, Yang D, Zhao Y, Xing H, Li X and Chen D 2018 *J. Appl. Phys.* **124** 065901

[41] Souchay D, Nentwig M, Günther D, Keilholz S, de Boor J, Zeugner A, Isaeva A, Ruck M, Wolter A U B, Büchner B and Oeckler O 2019 *J. Mater. Chem. C* **7** 9939

[42] Shi M Z, Lei B, Zhu C S, Ma D H, Cui J H, Sun Z L, Ying J J and Chen X H 2019 *Phys. Rev. B* **100** 155144

[43] Yan J Q, Liu Y H, Parker D, McGuire M A and Sales B C 2019 arXiv:1910.06273 [cond-mat.mtrl-sci]

[44] Hu C, Ding L, Gordon K N, Ghosh B, Li H, Lian S W, Linn A G, Tien H J, Huang C Y, Reddy P V S, Singh B, Agarwal A, Bansil A, Xu S Y, Lin H, Cao H, Chang T R, Dessau D and Ni N 2019 arXiv:1910.12847 [cond-mat.str-el]

# Supplementary Material: Pressure-induced Topological and Structural Phase Transitions in an Antiferromagnetic Topological Insulator*

CuiYing Pei(裴翠颖)[1***], Yunyouyou Xia(夏云悠悠)[1,2,3***], Jiazhen Wu(邬家臻)[4], Yi Zhao(赵毅)[1], Lingling Gao(高玲玲)[1], Tianping Ying(应天平)[4], Bo Gao(高波)[5], Nana Li(李娜娜)[5], Wenge Yang(杨文革)[5], Dongzhou Zhang(张东舟)[6], Huiyang Gou(缑慧阳)[5], Yulin Chen(陈宇林)[1,7,8], Hideo Hosono(细野秀雄)[4], Gang Li(李刚)[1,8**] and Yanpeng Qi(齐彦鹏)[1**]

[1] School of Physical Science and Technology, ShanghaiTech University, 393 Middle Huaxia Road, Shanghai 201210, China

[2] Shanghai Institute of Optics and Fine Mechanics, Chinese Academy of Sciences, Shanghai 201800, China

[3] University of Chinese Academy of Sciences, Beijing 100049, China

[4] Materials Research Center for Element Strategy, Tokyo Institute of Technology, 4259 Nagatsuta, Midori-ku, Yokohama 226-8503, Japan

[5] Center for High Pressure Science and Technology Advanced Research (HPSTAR), 1690 Cailun Road, Shanghai 201203, China

[6] Hawai'i Institute of Geophysics and Planetology, School of Ocean and Earth Science and Technology, University of Hawai'i at Manoa, Honolulu, Hawaii 96822 USA

[7] Department of Physics, Clarendon Laboratory, University of Oxford, Parks Road, Oxford OX1 3PU, UK

[8] ShanghaiTech Laboratory for Topological Physics, ShanghaiTech University, Shanghai 200031, China

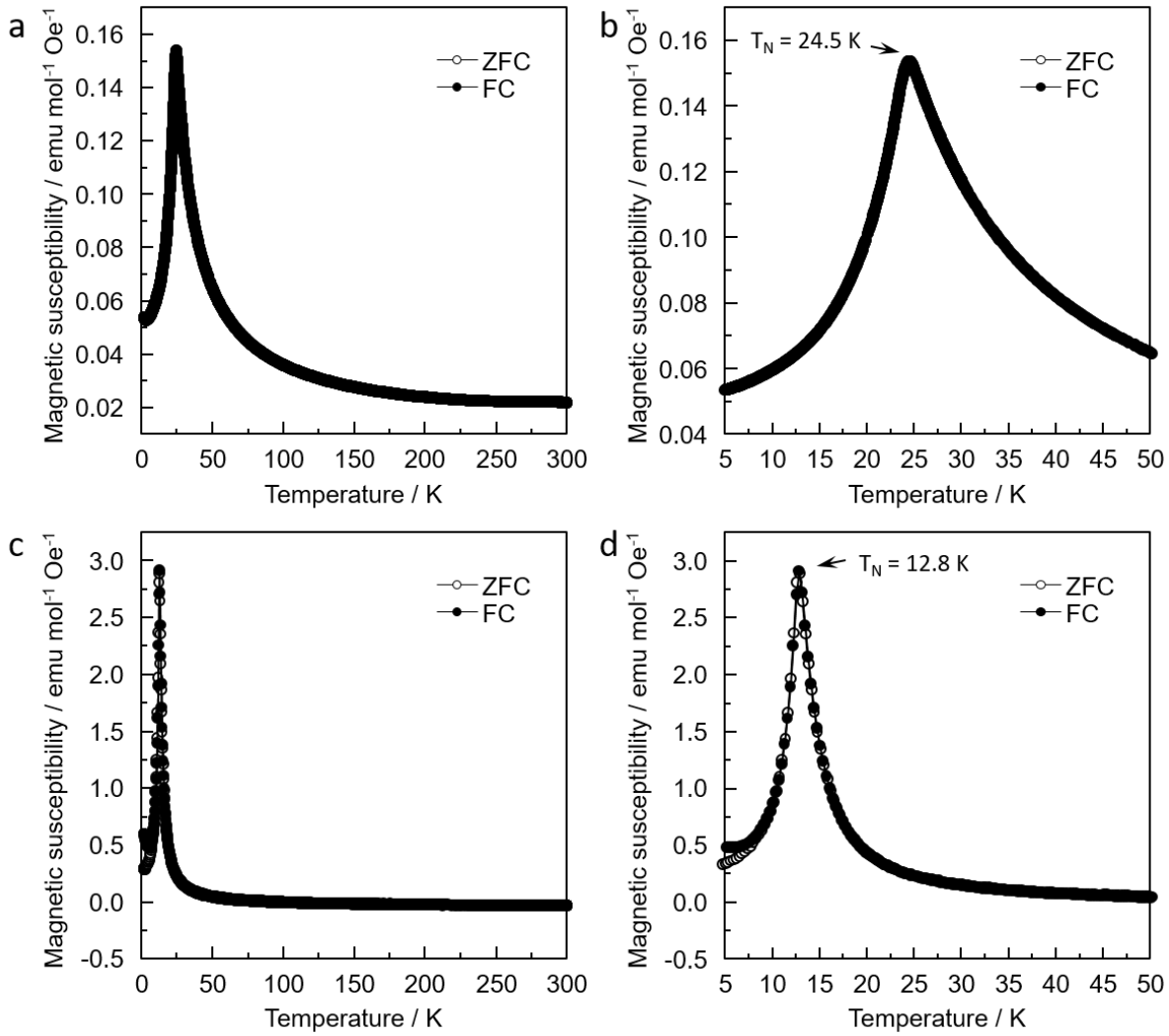


**Figure S1.** Field cooled (FC) and zero-field cooled (ZFC) temperature dependences of magnetic susceptibility $\chi$ measured at 1 T for the $MnBi_2Te_4$ crystals (a, b) and 50 Oe for $MnBi_4Te_7$ crystals (c, d) aligned with the magnetic field parallel (*H//c*) to the *c*-axis. The susceptibility data shows an AFM transition with $T_N$ = 24.5 K in $MnBi_2Te_4$ and $T_N$ = 12.8 K in $MnBi_4Te_7$.

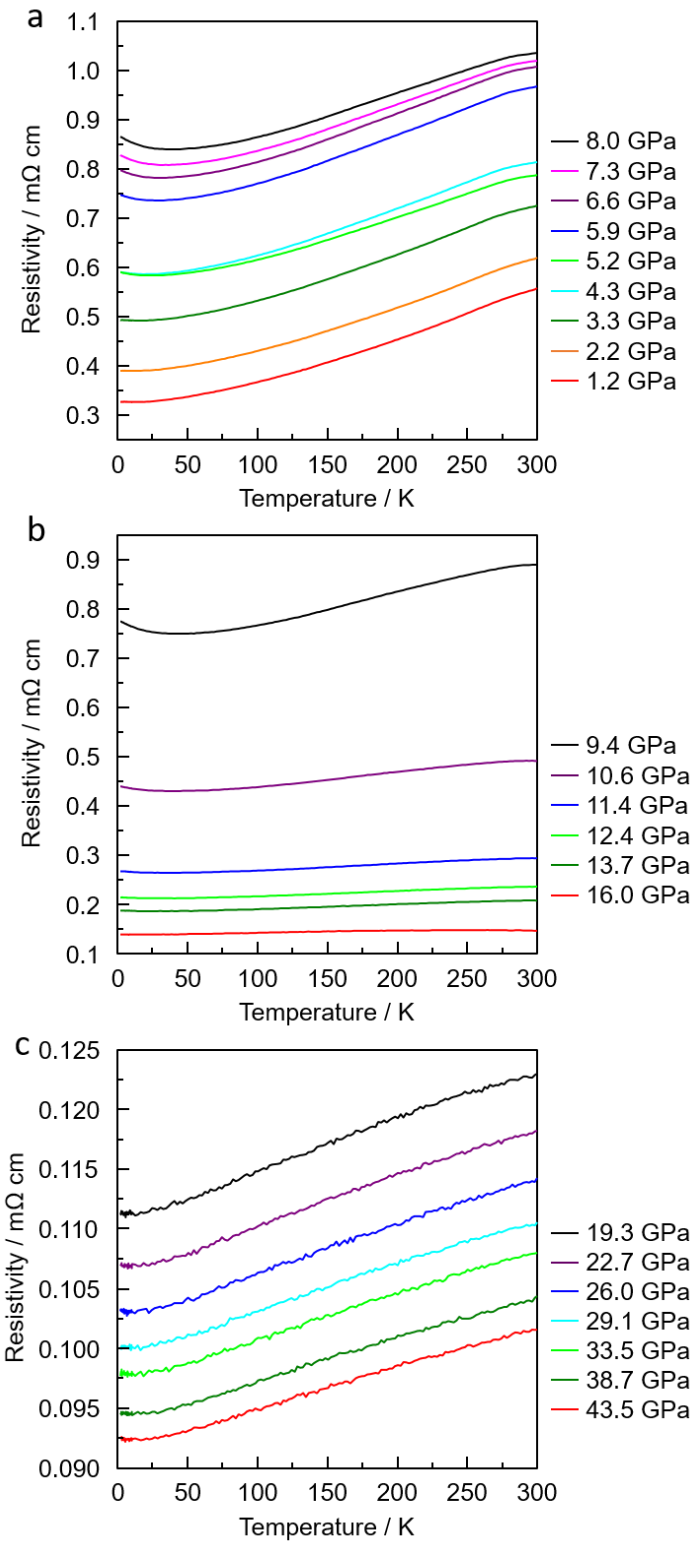


**Figure S2.** Electrical resistivity of $MnBi_4Te_7$ as a function of temperature for pressures up to 8.0 GPa (a), 16.0 GPa (b) and 43.5 GPa (c) in run II.

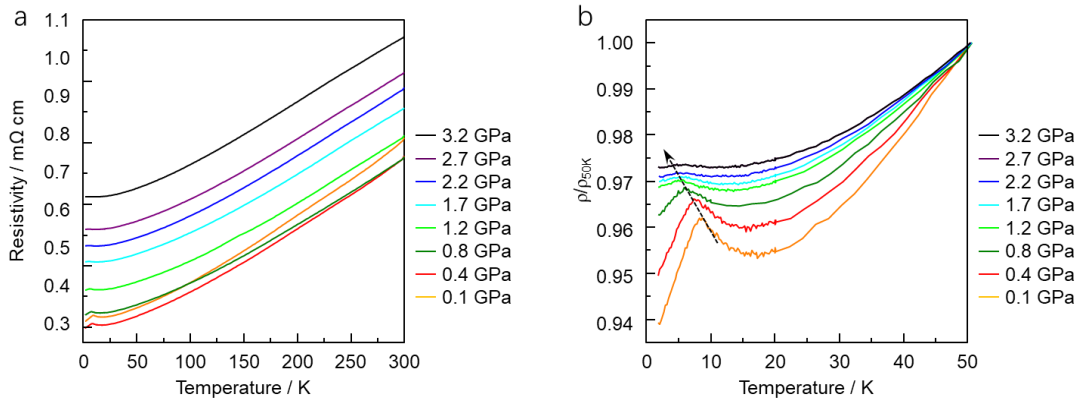


**Figure S3.** (a) Electrical resistivity of $MnBi_4Te_7$ as a function of temperature for pressures up to 3.2 GPa in run III; (b) Detail of the normalized resistivity of $MnBi_4Te_7$ as a function of temperature at various pressures to monitor the shift of the AFM transition kink.

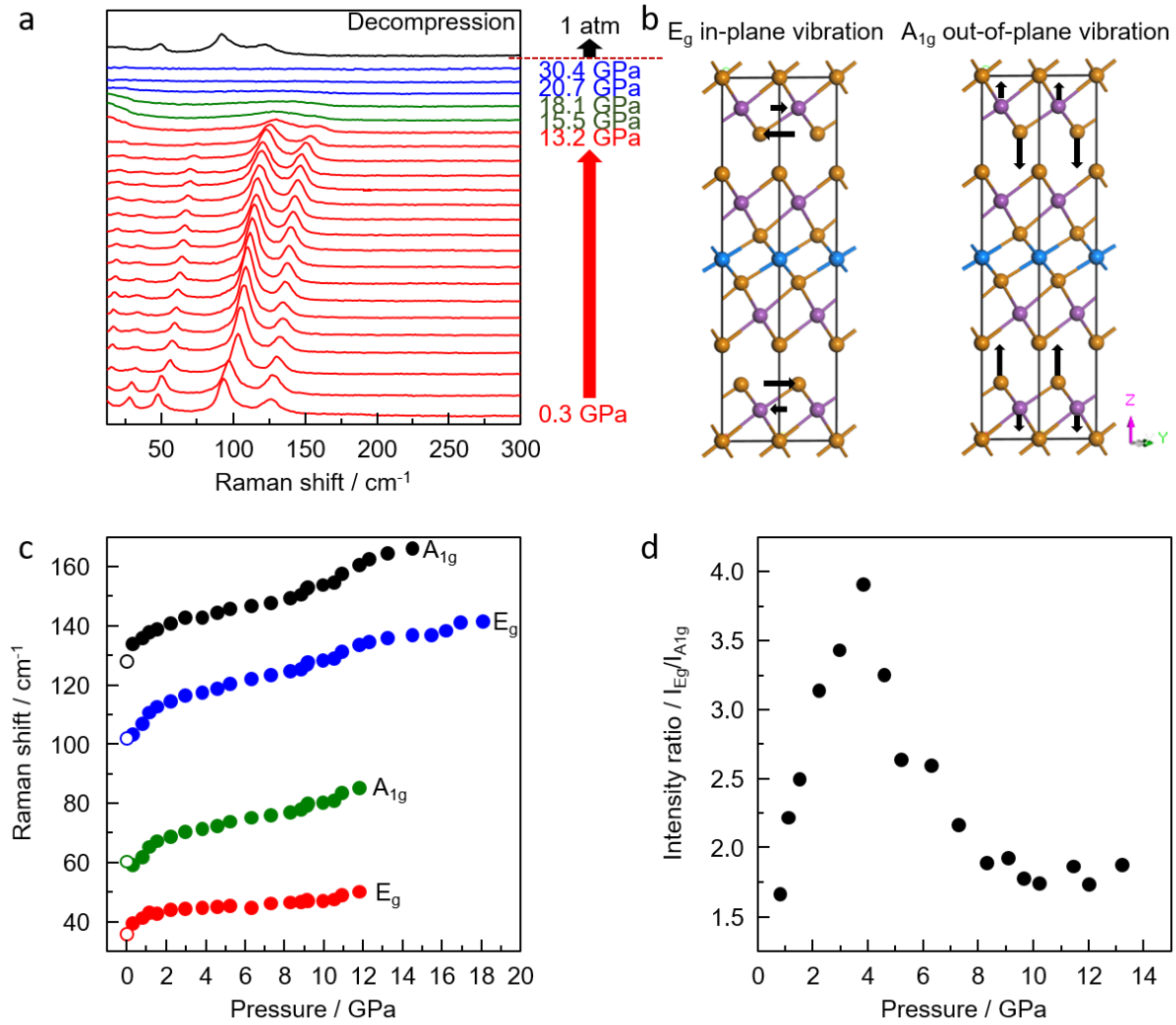


**Figure S4.** (a) Raman spectra at various pressure for $MnBi_4Te_7$; (b) Phonon mode symmetry and direction of vibration for $MnBi_4Te_7$; (c) Raman mode frequencies for $MnBi_4Te_7$ in compression (solid circle) and decompression (open circle); (d) Pressure

dependence of $I_{Eg}/I_{A1g}$ intensity ratio for $MnBi_4Te_7$. For accurate peak intensity comparison, the strong $E_g$ mode and $A_{1g}$ mode which show as 107.8 $cm^{-1}$ and 137.7 $cm^{-1}$ at 0.1 GPa, respectively is chosen. Peak intensity and peak position is obtained by Gaussian and Lorentzian mixed line shape fitting.

Raman spectra of $MnBi_4Te_7$ has been shown in Figure S4, and the vibration modes are in good agreement with previous reports.[1] With the increasing pressure, all the Raman modes shift toward higher frequencies. Lower wavenumber $E_g$ and $A_{1g}$ modes disappear first, accompanied by higher wavenumber $E_g$ and $A_{1g}$ modes become broad obviously over 11.1 GPa. No obvious phase transition is detected below 15.5 GPa, but over it, the high frequency $A_{1g}$ mode disappear and only weak high frequency $E_g$ mode maintains up to 18.1 GPa. It is inconsistent with the XRD results that the pressure of the onset of phase transition occured at 14.4 GPa and pure phase III appeared at 18.6 GPa. Similar to $MnBi_2Te_4$, the intensity ratio of in-plane and out-of-plane vibration mode is pressure dependent and the maxium $I_{Eg}/I_{A1g}$ shows at around 3.8 GPa.

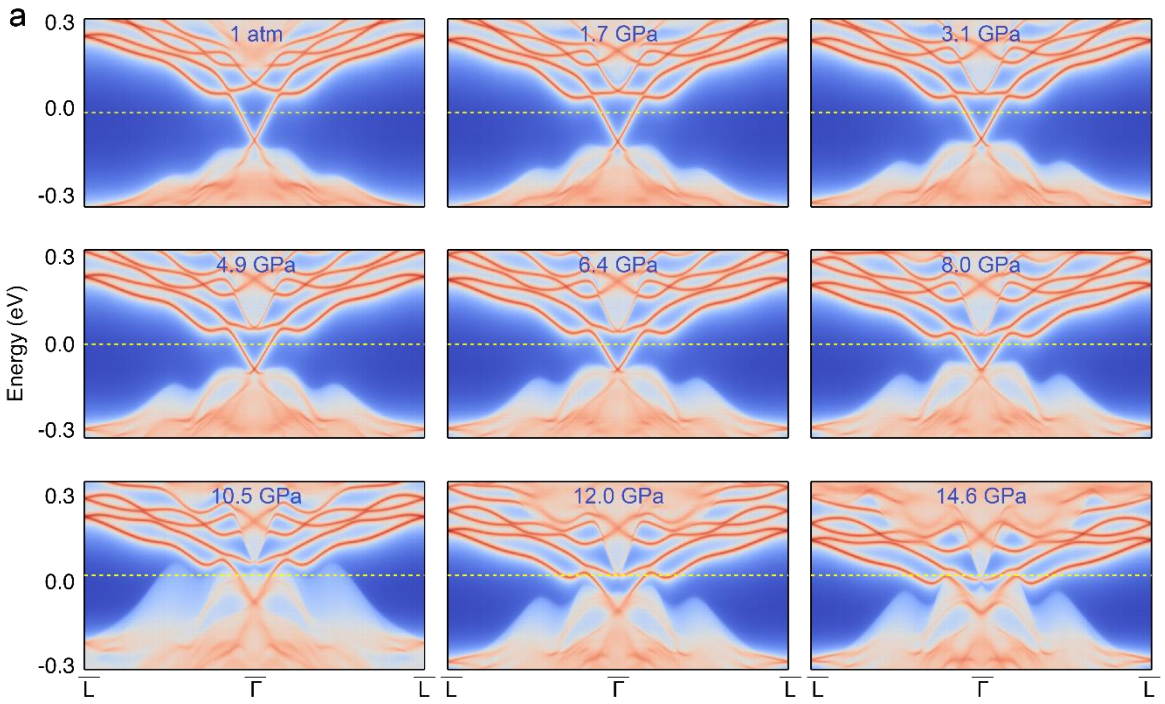

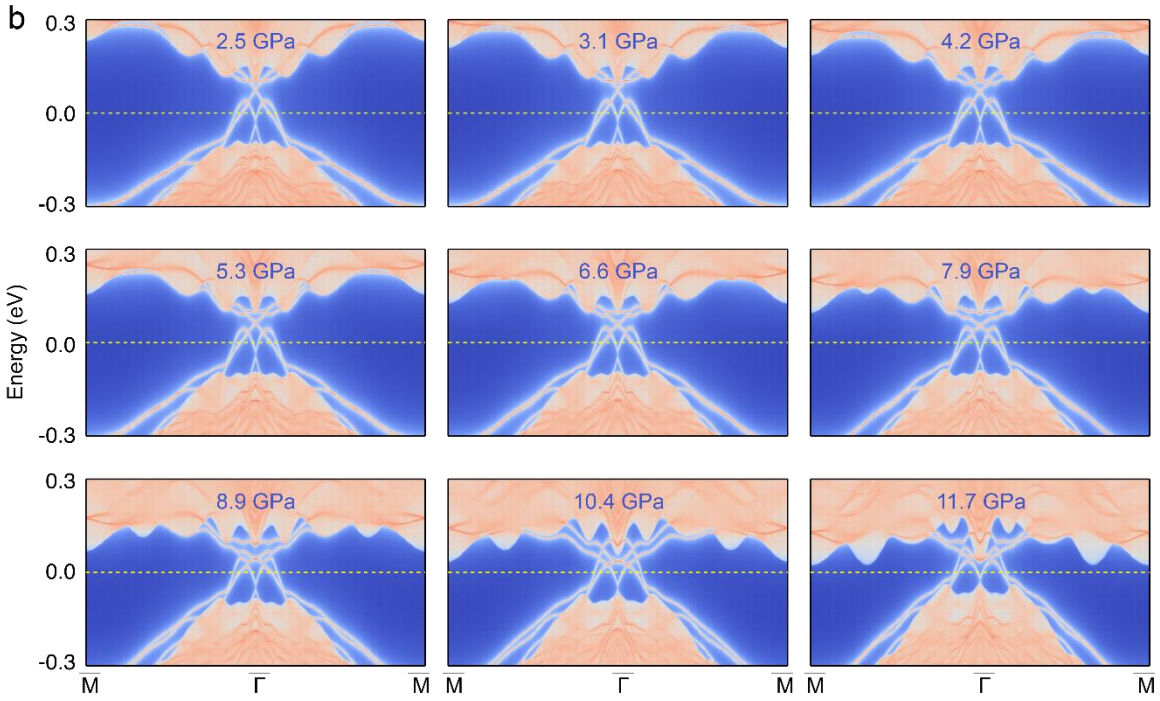


**Figure S5.** The gapless topological surface states on the effective time-reversal symmetry $\mathcal{S} = T\tau_{1/2}$ preserving surface, indicating stable nontrivial topology in the displayed pressure range. (a) The topological surface states on $(1\bar{1}0)$ of $MnBi_2Te_4$. (b) The topological surface states on (100) of $MnBi_4Te_7$.

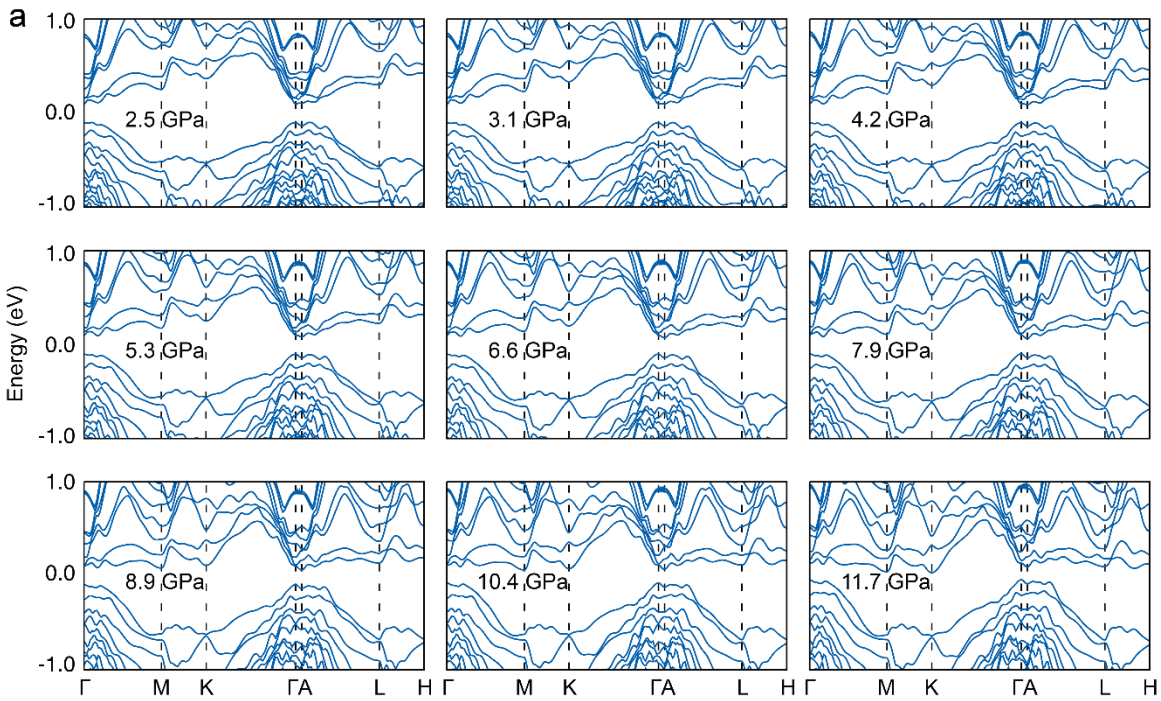

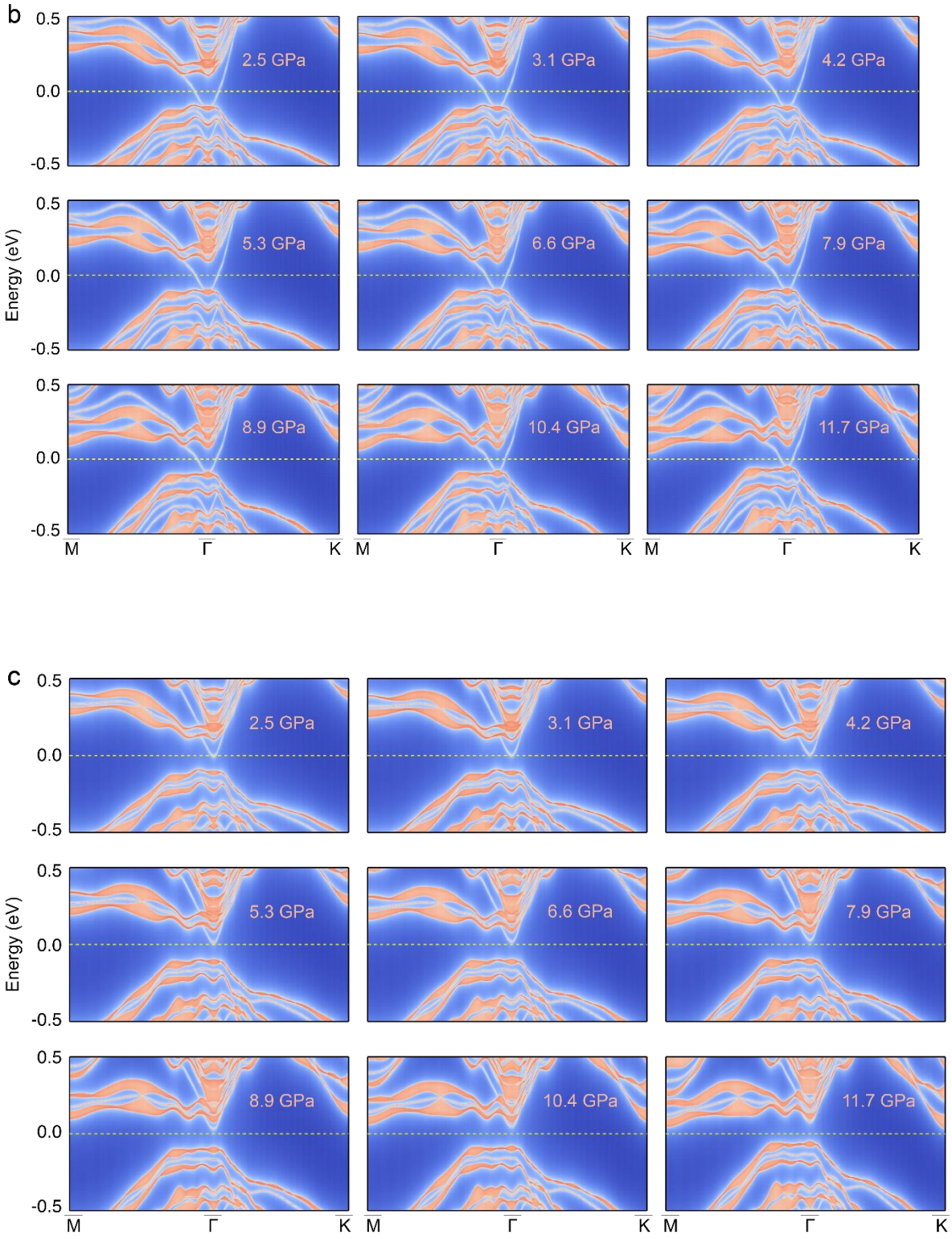


**Figure S6.** The bulk and surface electronic structures of $MnBi_4Te_7$ under different pressures. (a) The bulk electronic structure remains gapped under all applied pressures with roughly monotonic decrease of the global gap size in the whole Brillouin zone. (b) The topological surface states of (001) with $MnBi_2Te_4$ termination intersect the Fermi level under all examined pressures. (c) The topological surface states of (001) with $Bi_2Te_3$ termination gradually shrink above the Fermi level.

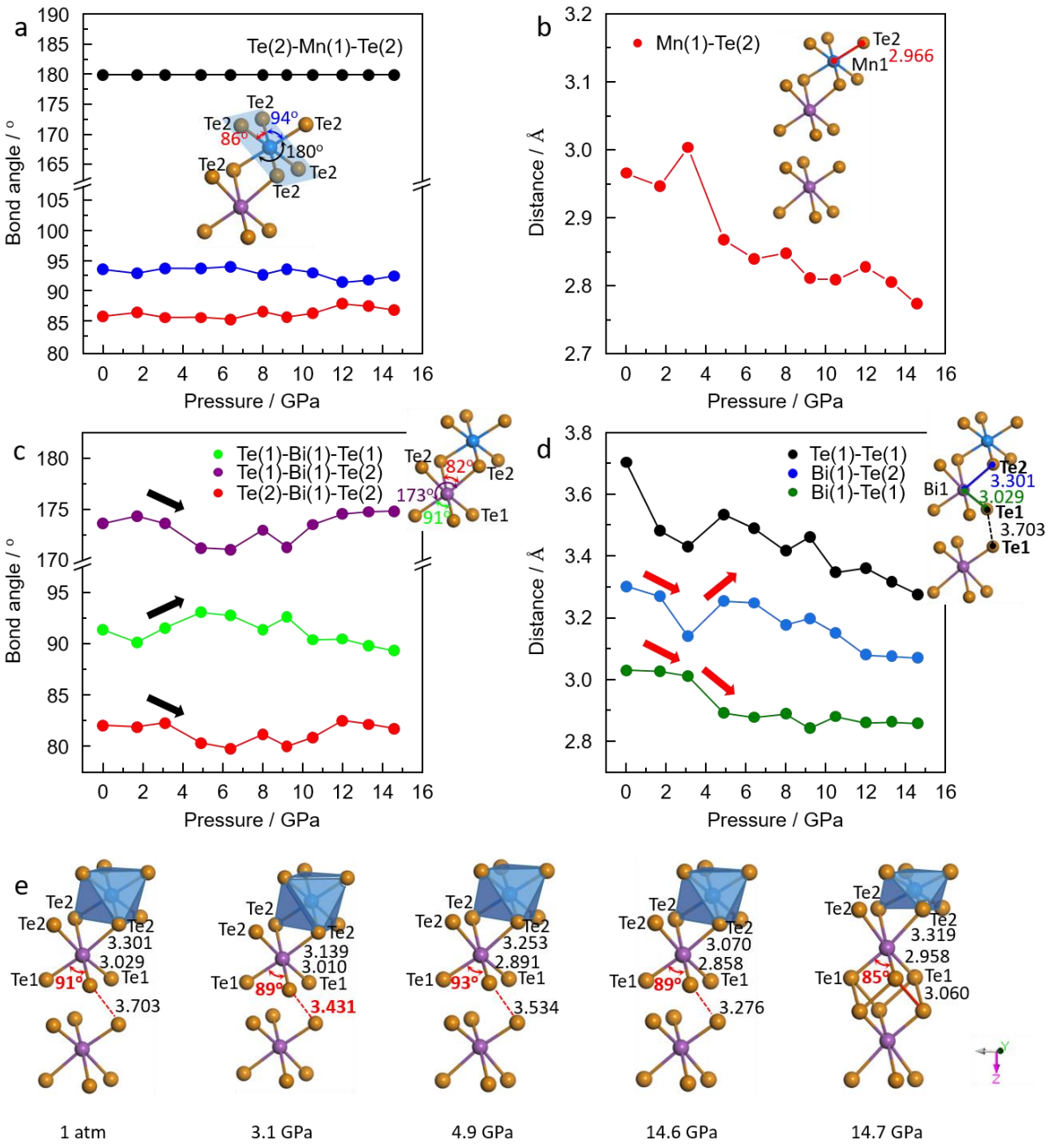


**Figure S7.** (a) Experimental bond angle of Te(2)-Mn(1)-Te(2) of $MnBi_2Te_4$ for *R-3m* under various pressures; (b) bond length of Mn(1)-Te(2) of $MnBi_2Te_4$ for *R-3m* under various pressures; (c) bond angle of Te(1)-Bi(1)-Te(1), Te(1)-Bi(1)-Te(2), Te(2)-Bi(1)-Te(2) of $MnBi_2Te_4$ for *R-3m* under various pressures; (d) bond length of Te(1)-Te(1), Bi(1)-Te(2), Bi(1)-Te(1) of $MnBi_2Te_4$ for *R-3m* under various pressures; (e) Structure evolution in the view of $MnTe_6$ and $BiTe_6$ octahedron based on Rietveld refinements of XRD result taken with X-ray wavelength $\lambda = 0.4340$ Å.

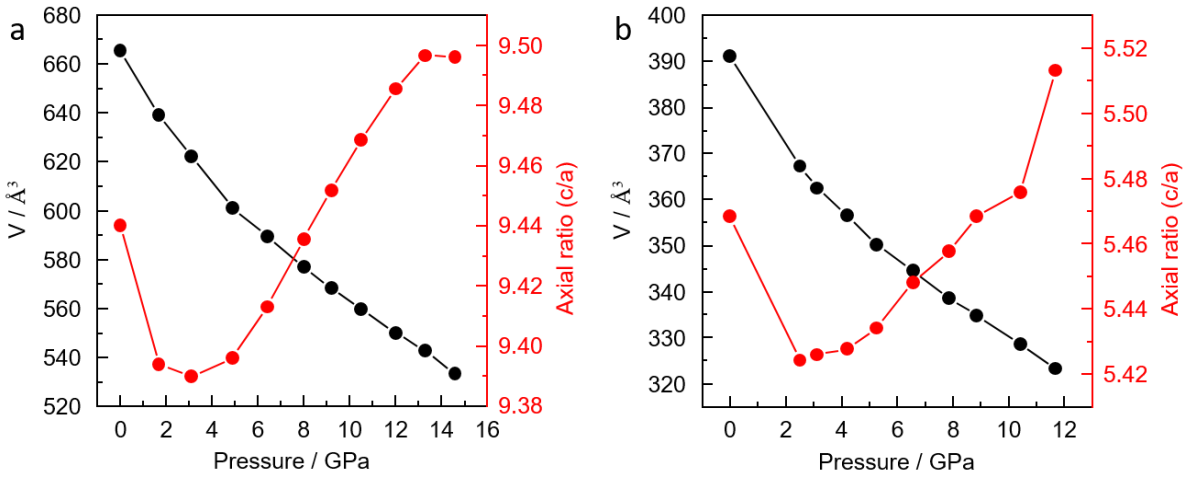


**Figure S8.** Pressure-dependence of experimental volume and axial ratio (c/a) of $MnBi_2Te_4$ (a) relative to *R*-3*m* phase and $MnBi_4Te_7$ (b) relative to *P*-3*m*1 phase, respectively.

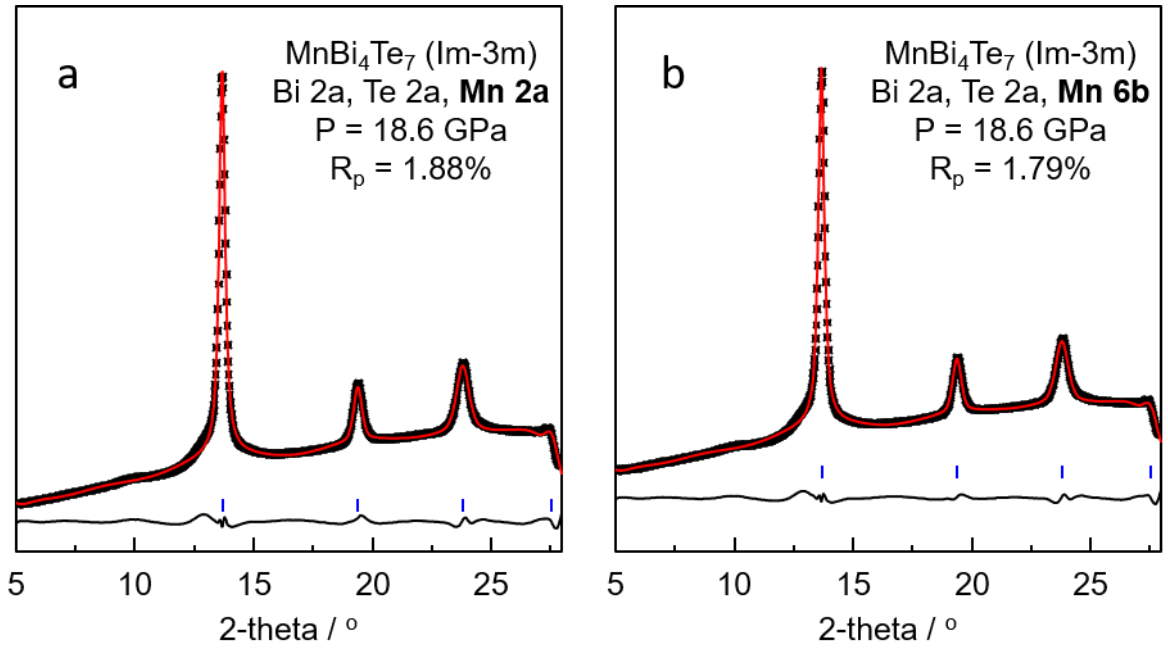


**Figure S9.** Typical Rietveld refinement of phase III of $MnBi_4Te_7$ obtained at 18.6 GPa. (a) Bi, Te and Mn atoms assigned on one Wyckoff position 2a in the crystallographic model I; (b) Bi, Te atoms assigned on 2a Wyckoff position and Mn atoms assigned on 6b Wyckoff position in the crystallographic model II. The experimental and simulated data were symbolled with black start and red line. The solid lines at the bottom are the residual intensities. The vertical bars indicate the peak positions.

Considering the close similarities, it is natural to suppose that $MnBi_4Te_7$ adopts the same structure evolution under high pressure. Nevertheless, an ambiguity in the space group assignment (*Im-3m*) of this new high-pressure phase still exists. The

crystallographic models have two types due to different assignments for the Mn atoms on the Wyckoff positions as shown in Figure S9.

**Table S1.** Structural parameters of $MnBi_4Te_7$ at 18.6 GPa at room temperature.

| | Model I | Model II |
|---|---|---|
| Crystal system | cubic | cubic |
| Space group | *Im-3m* (229) | *Im-3m* (229) |
| a | 3.6800(6) | 3.6800(2) |
| atoms position | Wyckoff (x y z) | Wyckoff (x y z) |
| Mn | 2a (0,0,0) | 6b (0.5,0,0) |
| Bi | 2a (0,0,0) | 2a (0,0,0) |
| Te | 2a (0,0,0) | 2a (0,0,0) |
| Residuals[a] / % | $R_{wp}$: 1.88% | $R_{wp}$: 1.79% |
| | $R_p$: 1.39% | $R_p$: 1.31% |

[a] $R_{wp}$ and $R_p$ as defined in GSAS[2]

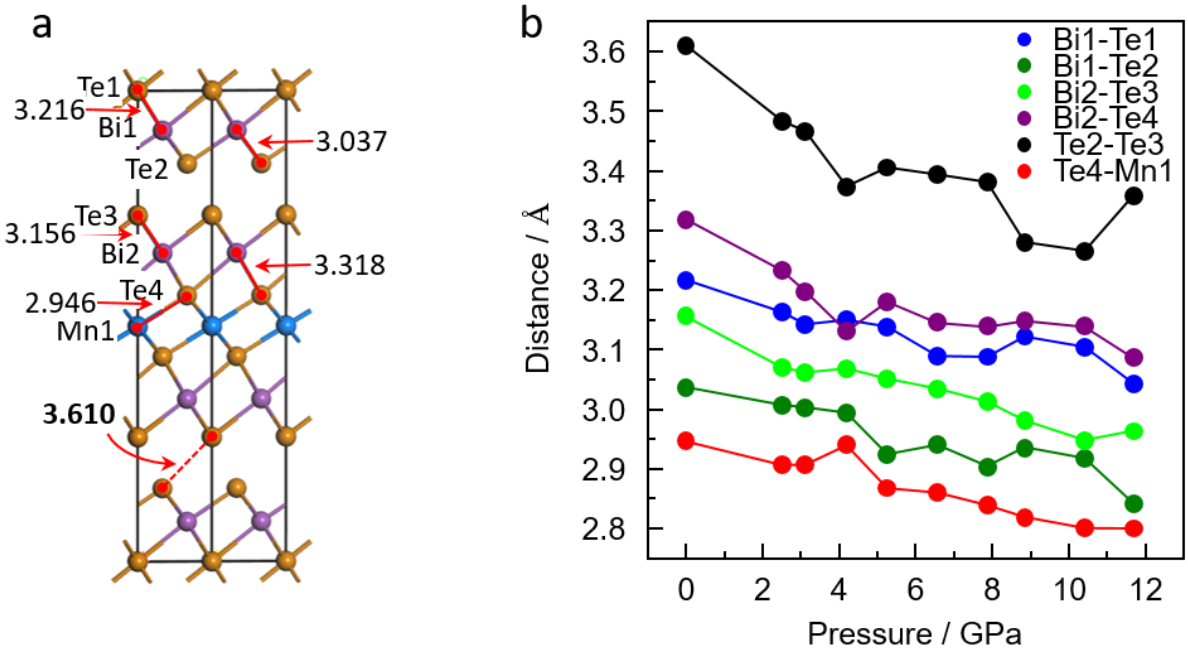


**Figure S10.** (a) unit cells of $MnBi_4Te_7$ at 1 atm; (b) Experimental atom distances of Bi1-Te1, Bi1-Te2, Bi2-Te3, Bi2-Te4, Te2-Te3 and Te4-Mn1 of $MnBi_4Te_7$ for *P-3m*1 under various pressures.

(1) Mal, P.; Bera, G.; Turpu, G. R.; Srivastava, S. K.; Gangan, A.; Chakraborty, B.; Das, B.; Das, P., Vibrational spectra of $Pb_2Bi_2Te_3$, $PbBi_2Te_4$, and $PbBi_4Te_7$ topological insulators: temperature-

dependent Raman and theoretical insights from DFT simulations. *Phys. Chem. Chem. Phys.* **2019,** *21*, 15030-15039.

(2) Larson, A. C.; Dreele, R. B. V., General structure analysis system (GSAS). *Los Alamos National Laboratory Report LAUR* **2004**, 86-748.